

# Multiscale simulation of powder-bed fusion processing of metallic alloys

S.M. Elahi<sup>a,b</sup>, R. Tavakoli<sup>a</sup>, A.K. Boukellal<sup>a</sup>, T. Isensee<sup>a,c</sup>, I. Romero<sup>a,b</sup>, D. Tournet<sup>a</sup>

<sup>a</sup>*IMDEA Materials, Madrid, Spain*

<sup>b</sup>*Universidad Politécnica de Madrid, E.T.S. de Ingenieros Industriales, Madrid, Spain*

<sup>c</sup>*Universidad Politécnica de Madrid, E.T.S. de Ingenieros de Caminos, Madrid, Spain*

---

## Abstract

We present a computational framework for the simulations of powder-bed fusion of metallic alloys, which combines: (1) CalPhaD calculations of temperature-dependent alloy properties and phase diagrams, (2) macroscale finite element (FE) thermal simulations of the material addition and fusion, and (3) microscopic phase-field (PF) simulations of solidification in the melt pool. The methodology is applied to simulate the selective laser melting (SLM) of an Inconel 718 alloy using realistic processing parameters. We discuss the effect of temperature-dependent properties and the importance of accounting for different properties between the powder bed and the dense material in the macroscale thermal simulations. Using a two-dimensional longitudinal slice of the thermal field calculated via FE simulations, we perform an appropriately-converged PF solidification simulation at the scale of the entire melt pool, resulting in a calculation with over one billion grid points, yet performed on a single cluster node with eight graphics processing units (GPUs). These microscale simulations provide new insight into the grain texture selection via polycrystalline growth competition under realistic SLM conditions, with a level of detail down to individual dendrites.

*Keywords:* Computational Modeling, Powder-bed fusion, Finite Elements, Phase-Field, CalPhaD

---

## 1. Introduction

Fusion-based additive manufacturing (AM) processes for metals combine a formidable breadth of interdependent physical phenomena [1]. In this context, Integrated Computational Materials Engineering (ICME) [2–5] offers a prominent pathway to accelerate the design of novel alloys and to optimize manufacturing processes, by reducing the dependence on experimental trial-and-error iterations. ICME heavily relies on linking multiple modeling techniques relevant to distinct length/time scales and/or different physical phenomena. Yet, despite the fact that a wide range of models has been established, the efficient bridging between models and between scales remains a major challenge.

The rapid deployment of metal additive manufacturing in the last decade has led to the development of many modeling approaches for powder-bed fusion processes [6–8]. At the macroscopic/process scale, multi-physics models have been developed in order to combine fluid and solid mechanics and thermal transport (conduction, convection, and radiation) during melting and solidification phenomena resulting from the moving heat source (e.g. laser or electron beam) above a powder bed [9–14]. These studies have demonstrated the importance of fluid flow within the melt pool — in particular, Marangoni convection and recoil pressure — on the formation of critical defects, such as poros-

ity, spattering, denudation, and balling [10–14]. The effect of the scanning strategy, e.g. the hatch pattern [12, 13], was also shown to have a key effect on the quality of the build. Scanning path, cross-section thickness, and the presence of additional lasers were also found to have a strong influence on residual stresses, which also exhibit significant differences between vertical (build) and horizontal directions [13]. Meso-scale phase-field (PF) models of the melting and solidification of powder particles were also shown to capture the effect of the heat source power and speed on the densification, defects, and surface morphology [15–17]. Three-dimensional PF simulations of polycrystalline grain structures at the melt pool scale were recently reported in the case of high growth velocities reaching absolute interfacial stability [18]. However, it remains limited to alloys and growth velocities that yield complete solute trapping and planar re-stabilization of the solid-liquid interface. As most metallic alloys develop dendritic or cellular microstructures during AM, grain growth competition typically involves complex mechanisms such as dendritic sidebranching and impingement of individual dendrite or cells [19, 20].

At the scale of the grain structure, the choice of the model often results in the classical trade-off between efficiency (and hence scale) and physics-based accuracy. Among coarse-grained, efficient approaches, those based on the kinetic Monte Carlo (KMC) method conveniently allow three-dimensional simulation at the

full melt pool scale, including multiple layers [21, 22]. However, they usually do not integrate some essential physics behind polycrystalline microstructure selection (e.g. the anisotropic growth kinetics and preferred growth directions of crystalline grains). Models based on meso-scale cellular automata (CA) coupled with macro-scale thermomechanics (e.g. using finite elements or differences) provide a good compromise between efficiency and physics-based considerations [23–29]. In such models, grains can be constructed from polyhedral building blocks, whose vertices mark the preferred crystallographic growth directions. Growth velocities in these directions follow simplified, yet physics-based, kinetic laws for crystal growth — e.g. using Ivantsov-based relations or power laws relying on local supersaturation or undercooling. As such, these models still include some adjustable phenomenological parameters. It was recently shown that polycrystalline growth can be predicted by CA-based models with an accuracy comparable to that of phase-field, as long as the cell size is adjusted to the length scale relevant to the grain growth competition — e.g. the “height” difference between the two competing grains [30] or the spacing between active secondary branches [31].

At the scale of dendritic/cellular arrays, most-accurate physics-based models require a numerical discretization commensurate with the microstructural scale of interest, and therefore result in computationally expensive simulations. Phase-field (PF) models are arguably the most accurate approach to simulate the evolution of morphologically complex interfaces based solely on thermodynamics and kinetics considerations [32–37]. The method has been particularly successful in the field of solidification, often using “mesoscale” interface formulations that remain faithful to the well-known sharp-interface problem even for diffuse interfaces much wider than the actual interface width or its capillary length [32, 36]. However, spatial discretization remains upward-bounded by the typical microstructural length scale, i.e. the local interface curvature [35, 38, 39]. Since dendrite tip radii can go down to a few tens of nanometers in fusion-based metal AM, this spatial discretization requirement makes quantitative simulations computationally demanding. Therefore, reported studies that have used PF to simulate solidification within an AM melt pool have been limited in size [40–44].

Computational approaches have been proposed that combine macroscopic thermal models with lower scale microstructure models [6–8]. Recent studies have used macroscopic thermal simulation of AM processing, in order to provide thermal conditions for lower scale PF simulations of solidification [40, 44–46]. Yet, while full melt pool simulations appear within reach using computationally-efficient parallelized implementations (see, e.g. [47]), PF simulations have been mostly re-

stricted to the growth of a handful of dendrites with thermal conditions relevant to a subset of the melt pool region [40, 44–46].

In this article, we present a multiscale modeling framework for powder-bed fusion processes, and demonstrate its capabilities focusing on the simulation of selective laser melting of Nickel-based superalloy Inconel 718. The modeling approach does not focus on melt pool fluid dynamics nor defect formation. Rather, a key objective is to obtain a sensible physics-based prediction of the key microstructural features (e.g. grain sizes, dendritic spacings, and chemical segregation between and within the grains) at the scale of the entire melt pool. The computational framework combines three main components. First, the CalPhaD method provides thermophysical properties of the alloy and its phase diagram. Then, a three-dimensional macroscale finite element (FE) model is used to assess the temperature field, with particular emphasis on the accurate description of the melt pool size and shape. Finally, using the FE-calculated temperature field, a quantitative phase-field (PF) simulation is performed along a two-dimensional slice (here using the most computationally demanding longitudinal slice) at the scale of the entire melt pool. By linking the models with one another, we ensure that microstructure simulations are performed using realistic alloy and process parameters — and importantly the actual resulting melt pool size and shape.

## 2. Methods

The multiscale simulation approach presented here relies on three major components, namely: (1) computational thermodynamics (CalPhaD) to calculate temperature-dependent properties of complex alloys and their phase diagram, (2) macroscale (FE) thermal simulation of the powder-bed fusion, and (3) microscale (PF) simulation of microstructure development by crystal growth within the melt pool. Macro- and microscale simulations are coupled through the temperature field, estimated within a two-dimensional slice in the vicinity of the melt pool, and used as input to the phase-field simulations. The latter are upscaled using massive parallelization on Graphics Processing Units (GPUs) in order to make them applicable at the full melt pool scale, without compromising their accuracy, i.e. retaining the required grid size of a few nanometers. The key features of the resulting computational framework are schematized in Figure 1 and details are presented in the following subsections.

### 2.1. Computational thermodynamics of multicomponent alloy

Thermodynamic properties used in the FE and PF simulations are calculated using the CalPhaD (CAL-culation of PHase Diagrams) method. The method

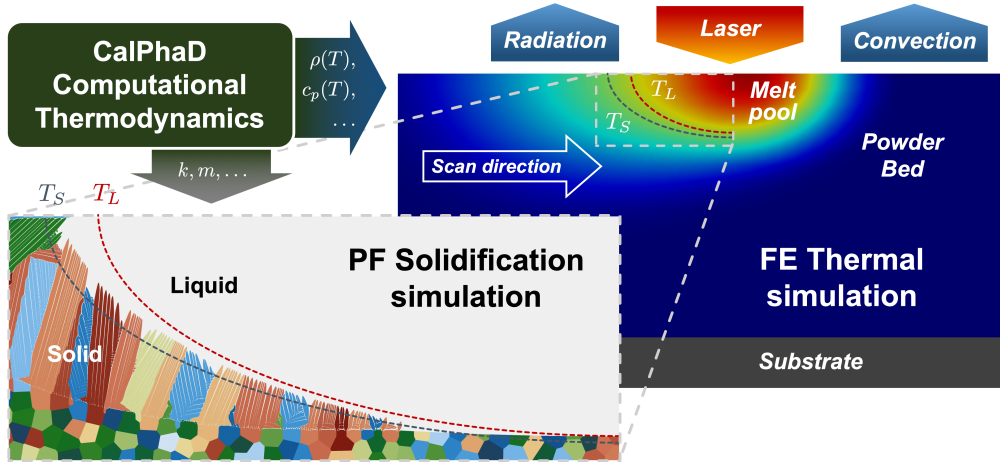


Figure 1: Main components of the multiscale modeling strategy, namely: CalPhaD thermodynamics, Finite Elements thermal simulation of SLM processing, and Phase-Field solidification simulation at melt pool scale.

is based on the global minimization of the free energy using databases describing the free energies of individual phases. Extensive databases thus allow calculating thermodynamic equilibria, i.e phase diagrams, for complex multicomponent alloys, and therefore to study the effect of individual alloying element variation.

### 2.1.1. Temperature-dependent alloy properties

We calculated alloy properties as a function of temperature assuming complete equilibrium, i.e. a lever rule solidification path, but the methodology would be just as readily applicable considering alternative assumptions, e.g. Gulliver-Scheil [48]. In particular, within a temperature range spanning all phase transformations, here from 250 K to 5000 K, we estimated the temperature-dependent density,  $\rho(T)$ , as well as the enthalpy per unit mass,  $h(T)$ . From the latter, we calculated an effective heat capacity  $c_p(T) = \partial h(T)/\partial T$  that includes not only the actual heat capacity but also the enthalpies (latent heat) of transformations in the relevant temperature ranges. From the tabulation of the fraction of liquid versus temperature, one can also extract the key transformation temperatures, namely liquidus ( $T_L$ ), solidus ( $T_S$ ) and boiling ( $T_V$ ) temperatures.

In particular, we apply the approach to a multicomponent Inconel 718 (IN718) superalloy, of composition listed in Table 1, using the software ThermoCalc with Ni-alloys database TCNI8. In the interest of computational efficiency, the resulting  $h(T)$  and  $\rho(T)$  used in the FE calculations are approximated by piecewise linear functions (see Section 3.1). CalPhaD-calculated properties can also be complemented by any further temperature-dependent property from other sources, such as illustrated here using a thermal conductivity,  $\kappa(T)$ , from the literature [49].

Table 1: Chemical composition of superalloy Inconel 718

Element	Ni	Cr	Nb	Mo	Ti	Al
Weight %	50.0	17.0	4.75	2.8	0.65	0.2

### 2.1.2. Phase diagram and pseudo-binary approximation

CalPhaD is also used to calculate phase diagram features for the PF simulations. As described in section 2.4, we use a reference quantitative phase-field model for binary alloy solidification. Therefore, the alloy is approximated by a pseudo-binary Ni-5wt%Nb, but the coupling approach could be readily extended without loss of generality to further models, e.g. using models for multicomponent [50–52] and/or incorporating rapid solidification effects [53–58]. Solute trapping is intentionally left out of the current scope, such that the solid-liquid interface is assumed to remain close to thermodynamic equilibrium, with local deviation from the phase diagram solely due to solute and curvature effects. Consequently, to keep simulations quantitative, applications of the methodology are limited to a scan velocity at which the solute trapping is negligible (section 2.5). We focus specifically on Niobium because it is one of the solute elements in IN718 that exhibits the highest segregation during solidification, thus playing a key role in the formation of secondary intermetallic phases as well as in the hot cracking susceptibility of highly segregated grain boundaries.

There are several different ways to approximate of a multicomponent alloy as a pseudo-binary system. The most straightforward route is to directly consider the actual binary Ni-Nb system at the relevant Nb concentration (see, e.g., [40]). However, in the scope of a coupling of thermal fields while using thermophysical properties of the full alloy, this may lead to an important mismatch in transformation temperatures (e.g.  $T_L$ ,  $T_S$ ) between FE (full alloy) and PF (pseudo-

binary) calculations. Instead, here we aim at closely matching the liquidus temperature  $T_L$ , as well as the solute partitioning of Nb at the solid-liquid interface for a temperature close to  $T_L$ . To do so, we use CalPhaD (ThermoCalc, TCNI8) to compute the thermodynamic equilibrium of the complete alloy (Table 1) at  $T = T_L$ . At this point, we estimate the solute partition coefficient of Niobium,  $k = c_s/c_l$ , with  $c_s$  and  $c_l$  the respective concentration (weight) of Nb in the solid and liquid phase, and the liquidus slope with respect to the Nb concentration,  $m = \partial T_L / \partial c$ . Then, we calculate the corresponding (fictitious) pure solvent melting temperature,  $T'_M$ , and the solidus temperature,  $T'_S$ , assuming a linearized phase diagram, i.e. using  $T_L = T'_M + mc_\infty$  and  $T'_S = T'_M + (m/k)c_\infty$ , with  $c_\infty = 5\text{wt\%Nb}$  the nominal alloy solute concentration considered in the pseudo-binary approximation. (Here, prime symbols on  $T'_M$  and  $T'_S$  denote this pseudo-binary approximation.) Hence, this method may lead to some discrepancy in terms of the linearized  $T'_M$  and  $T'_S$  (see section 3.1) but it has the key advantage of retaining an accurate description of solute partitioning and interface equilibrium in the vicinity of  $T = T_L$  as well as a matching of temperature  $T_L$ . Other parameters, such as the solid-liquid interface Gibbs-Thomson coefficient or the liquid solute diffusivity are extracted or calculated from literature data (see section 2.5.3 and Table 3).

## 2.2. Macroscopic thermal simulations

We consider the thermal problem of a moving heat source above a powder bed. Neglecting mechanics, in particular fluid flow, is expected to have a strong influence. However, for printing in conduction mode, a thermal model is expected to provide a reasonable estimate of the temperature profile in and around the melt pool.

### 2.2.1. Thermal problem

Considering a bounded domain  $\Omega$  in  $\mathbb{R}^3$ , the governing equation for the heat transfer problem can be written as

$$\rho(T) c_p(T) \dot{T}(\mathbf{x}) = \nabla \cdot (\kappa(T) \nabla T), \quad \mathbf{x} \in \Omega \quad (1)$$

where  $T$  denotes the temperature,  $\rho$  the density,  $c_p$  the specific heat at constant pressure,  $\kappa$  the scalar (i.e. isotropic) conductivity of the material. Material properties, namely  $\rho$ ,  $c_p$ , and  $\kappa$ , are temperature-dependent, and hence a function of the location  $\mathbf{x}$  and time  $t$ .

Equation (1) does not have any volumic heat source term, but the laser beam is modeled by a 2D heat flux applied on the top surface of the powder bed. A standard Gaussian model is used that assumes a heat input that is symmetric with respect to the laser beam

axis and total irradiance

$$I = \frac{2AP}{\pi w^2} \exp\left(-\frac{2r^2}{w^2}\right) \quad (2)$$

where  $A$  is the absorptivity of the powder bed,  $P$  is the laser power,  $w$  is the laser beam diameter, and  $r$  is the radial distance from the center of the laser beam.

Along external boundaries, convection and radiation are considered. The convective heat transfer is modeled as

$$q_c(T) = h_c(T - T_{\text{ext}}) \quad (3)$$

where  $h_c$  is the convective heat transfer coefficient and  $T_{\text{ext}}$  is the temperature of the surrounding environment. Due to the high temperatures reached during laser melting, radiation is an important heat loss mechanism, which is modeled using the Stefan-Boltzmann law, with the radiative heat flux expressed as

$$q_r(T) = \sigma \epsilon (T^4 - T_{\text{ext}}^4) \quad (4)$$

where  $\sigma$  is the Stefan-Boltzmann constant and  $\epsilon$  is the material emissivity. Finally, at the bottom of the domain, a substrate material is considered to exchange heat via conduction with the powder bed and the solidified material, and a Dirichlet boundary condition of the form  $T = T_{\text{ext}}$  is set at the bottom of the substrate.

### 2.2.2. Material addition, phase change, and resulting properties

The material above the substrate can take three different “states”: Powder, Solid, and Fluid. The “powder” state is actually used for the powder bed, which is a combination of powder particles and gas, with homogenized properties reflecting that of the solid, gas, and morphological descriptors of the powder bed (e.g. average particle size, packing factor, etc.) as described in the following paragraphs. After the activation of a new layer (see section 2.2.3), the initial state of the added material is powder. At each time step, when the temperature of an element exceeds the alloy liquidus temperature,  $T_L$ , a transition occurs from powder to fluid state. Subsequently, the state of a fluid material point whose temperature becomes lower than the solidus temperature,  $T_S$ , is switched from fluid to solid.

The state of a point can change several times between fluid and solid depending on the local thermal history. However, once an element has switched from its initial powder state to a dense state, its properties remain those of a dense material, for the rest of the simulation. The subsequent changes between solid and fluid states are intrinsically represented by the temperature-dependent properties via their variations upon phase transformation (see Section 3.1 and Figure 3). The latent heat of transformations are not explicitly introduced in Eq. (1). Instead, the model uses an effective heat capacity, calculated as  $c_p(T) = \partial h(T) / \partial T$  for the entire temperature range,

which therefore incorporates the effect of these transformations. In practice, we use piecewise linear fits of the CalPhaD calculated  $h(T)$  and  $\rho(T)$  and we use the high-slope region of  $h(T)$  just above  $T_V$  for any temperature  $T \geq T_V$  (see later Figure 3). This way, the critical effect of evaporative cooling [59] is incorporated phenomenologically and the temperature saturates naturally when  $T$  exceeds  $T_V$ , without artificial increase of thermal conductivity [60] or reduction of the heat source term [61] in the vicinity of the evaporation temperature.

Temperature-dependent properties of the dense material are those calculated from CalPhaD or extracted from the literature. Properties of the powder bed are evaluated from those of the dense material, the surrounding gas, as well as additional descriptors of the powder morphology and packing. The density of the powder bed,  $\rho_p$ , is estimated using a classical rule of mixture

$$\rho_p = (1 - \xi)\rho_s + \xi\rho_g \quad (5)$$

where  $\xi$  is the porosity of the powder bed, and  $\rho_s$  and  $\rho_g$  are densities of bulk material and gas atmosphere (here: Argon), respectively. For the thermal conductivity of the powder bed, we use the model proposed by Sih and Barlow [62], derived from the Zehner-Schlünder-Damköhler equation [63, 64] assuming spherical particles and expressed as

$$\frac{\kappa_p}{\kappa_g} = \left(1 - \sqrt{1 - \xi}\right) \left(1 + \xi \frac{\kappa_r}{\kappa_g}\right) + \sqrt{1 - \xi} \left\{ \frac{2}{1 - \frac{\kappa_g}{\kappa_s}} \left[ \frac{1}{1 - \frac{\kappa_g}{\kappa_s}} \ln \left( \frac{\kappa_s}{\kappa_g} \right) - 1 \right] + \frac{\kappa_r}{\kappa_g} \right\} \quad (6)$$

where  $\kappa_p$ ,  $\kappa_s$ , and  $\kappa_g$  are conductivity of the powder bed, bulk material, and gas, respectively. The thermal conductivity due to radiation among particles,  $\kappa_r$ , is

$$\kappa_r = 4F\sigma T^3 d \quad (7)$$

where  $F$  is a view factor, here assumed equal to 1/3 [62, 63], and  $d$  is the average diameter of powder particles.

### 2.2.3. Numerical implementation

The thermal model described above was solved numerically in three dimensions using an in-house finite element code (IRIS) and a material library (MUESLI [65]) implemented in C++ programming language. A Galerkin method employing hexahedral elements was used to discretize the initial boundary value problem in space. The resulting semidiscrete equations were integrated in time with an implicit Backward-Euler method [66].

Elements for all layers are initially created, including those to be activated at later stages. They are activated progressively whenever new layers are deposited. The successive activation of layers is repeated with a

latency time between them that either represents the time for new powder application or provides sufficient time for the material to cool down to room temperature.

### 2.3. Macroscale to microscale coupling

Since thermal diffusivity in metals is several orders of magnitude higher than solute diffusivities, the kinetics of microstructural development within the melt pool is typically limited by the diffusion of species. Hence, we use the common assumption that the phase transformation does not have a significant effect on the temperature field, such that we can decouple the computation of the temperature field and that of the solidification within the melt pool. This results in a one-way coupling via the temperature field, which is calculated by FE and then imposed in the PF simulation.

The resulting PF simulations (see section 2.4) are rigorously analogous to those using the classical one-dimensional frozen temperature approximation [39], but imposing a different temperature field  $T(\mathbf{x}, t)$ . We extract this 2D temperature field within the longitudinal section of the sample along the laser path. For the sake of simplicity and computational efficiency, we use an analytical approximation of the temperature field. The selected expression aims at an approximate yet reasonable description of the temperature field in the region where it matters most for the development of the microstructure, namely between liquidus and solidus temperatures. Hence, we approximate solidus and liquidus isotherms as two ellipses

$$r_L(\theta) = \sqrt{\frac{(l_L d_L)^2}{(d_L \cos(\theta))^2 + (l_L \sin(\theta))^2}} \quad (8)$$

$$r_S(\theta) = \sqrt{\frac{(l_S d_S)^2}{(d_S \cos(\theta))^2 + (l_S \sin(\theta))^2}} \quad (9)$$

where  $r_L$  and  $r_S$  are the respective radii of the  $T = T_L$  and  $T = T_S$  ellipses as a function of the angle from the top surface

$$\theta = \tan^{-1} \left| \frac{y - y_0}{x - x_0} \right| \quad (10)$$

with  $(x_0, y_0)$  the center of the ellipses (see Figure 2a). Here,  $x_0$  is the location at which the melt pool is deepest, which may be slightly shifted backwards from the center of the heat source. Melt pool dimensions appear explicitly in Eqs (8) and (9) in the form the length ( $l_L$ ,  $l_S$ ) and depth ( $d_L$ ,  $d_S$ ) of the corresponding solidus (subscript  $S$ ) and liquidus ( $L$ ) isotherms. The resulting temperature field is then interpolated linearly between  $T_L$  and  $T_S$ , i.e. between  $r_L(\theta)$  and  $r_S(\theta)$  at a given  $\theta$ , as (Figure 2b)

$$T(r, \theta) = T_L + (T_0 - T_L) \frac{r - r_L(\theta)}{r_S(\theta) - r_L(\theta)}. \quad (11)$$

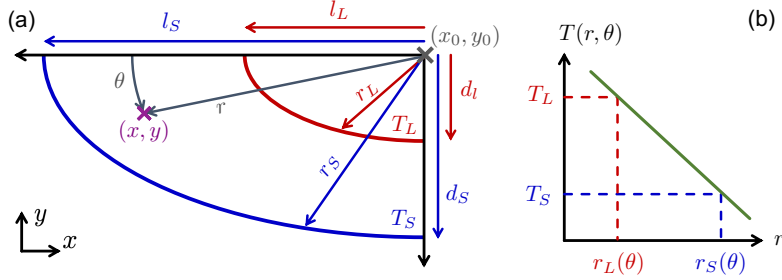


Figure 2: Schematics of the elliptic temperature field approximation.

One advantage of this expression is that it involves only four adjustable parameters ( $l_L$ ,  $l_S$ ,  $d_L$ ,  $d_S$ ), which can be measured directly and hence monitored automatically from the FE results. An underlying assumption is that the deepest point of the  $T_S$  and  $T_L$  isotherms are aligned on the same  $x_0$ . However, this is often the case since the two isotherms tend to be close to each other at the bottom of the melt pool (see Figs 4-5).

Even though we only illustrate the method for the longitudinal cross section with a steady temperature profile moving at constant velocity, the method is readily usable for any cross section or temperature field, including time-dependent temperature fields. Moreover, one can also easily substitute the proposed analytical expression by an efficient interpolating scheme directly estimating  $T(\mathbf{x}, t)$  from the FE results.

#### 2.4. Microscale modeling of microstructure growth in the melt pool

##### 2.4.1. Phase-field model

We consider a classical quantitative PF model for dilute binary alloy solidification [39]. To reduce the sensitivity of results to spatial grid size, we make use non-linear preconditioning of PF equation [67]. The final form of PF equations in two spatial dimensions is [19]:

$$\begin{aligned} \left(1 - \frac{T - T_0}{mc_l^0}\right) a_s(\alpha)^2 \frac{\partial \psi}{\partial t} = & \\ \nabla [a_s(\alpha)^2] \cdot \nabla \psi + a_s(\alpha)^2 \left[ \nabla^2 \psi - \phi \sqrt{2} |\nabla \psi|^2 \right] & \\ - \frac{\partial}{\partial x} \left[ a_s(\alpha) a'_s(\alpha) \frac{\partial \psi}{\partial y} \right] + \frac{\partial}{\partial y} \left[ a_s(\alpha) a'_s(\alpha) \frac{\partial \psi}{\partial x} \right] & \\ + \sqrt{2} \phi - \sqrt{2} \lambda (1 - \phi^2) \left( U + \frac{T - T_0}{mc_l^0(1 - k)} \right) & \end{aligned} \quad (12)$$

$$\begin{aligned} \left( \frac{1+k}{2} - \frac{1-k}{2} \phi \right) \frac{\partial U}{\partial t} = & \\ \nabla \cdot \left( \tilde{D} \frac{1-\phi}{2} \nabla U + [1 + (1-k)U] \frac{(1-\phi^2)}{4} \frac{\partial \psi}{\partial t} \frac{\nabla \psi}{|\nabla \psi|} \right) & \\ + [1 + (1-k)U] \frac{(1-\phi^2)}{2\sqrt{2}} \frac{\partial \psi}{\partial t} & \end{aligned} \quad (13)$$

where  $T$  is the temperature field,  $\phi$  is the classical phase-field variable (+1 in the solid and -1 in the liquid),  $\psi$  is the preconditioned phase-field variable with  $\phi(x, y, t) = \tanh(\psi(x, y, t)/\sqrt{2})$ ,  $\alpha = \arctan(\partial_y \psi / \partial_x \psi)$  is the angle between the solid-liquid interface normal and a fixed reference direction,  $U = \frac{1}{1-k} \left( \frac{2c/c_l^0}{1-\phi+k(1+\phi)} - 1 \right)$  is the dimensionless solute supersaturation, with  $c$  the solute concentration field,  $c_l^0 = c_\infty/k$  the solute concentration of a flat interface at the reference (solidus) temperature  $T_0$  for an alloy of nominal solute concentration  $c_\infty$ ,  $k$  is the interface solute partition coefficient and  $m$  is the slope of the liquidus line. In Eqs (12)-(13), space is scaled in units of the diffuse interface width,  $W$ , and time is in units of the relaxation time,  $\tau_0$ , at the temperature  $T_0$  [39]. Considering that interpolation functions used in (12) and (13) are determined based on the thin-interface asymptotic analysis [38, 39], their solutions will remain quantitative while using  $W$  much larger than the capillarity length. The capillarity length,  $d_0$ , is expressed at  $T_0$  as  $d_0 = \Gamma/(|m|c_\infty(1/k-1))$ , where  $\Gamma$  denotes the Gibbs-Thomson coefficient of the solid-liquid interface. The non-dimensional value for the liquid diffusion coefficient,  $\tilde{D}$ , and the coupling factor,  $\lambda$ , are computed according to

$$\tilde{D} = \frac{D\tau_0}{W^2} = a_1 a_2 \frac{W}{d_0} \quad (14)$$

$$\lambda = a_1 \frac{W}{d_0} \quad (15)$$

where  $D$  is the liquid diffusion coefficient (Eq. (13) neglects diffusion in the solid phase),  $a_1 = 5\sqrt{2}/8$ , and  $a_2 = 47/75$ . The standard form of the fourfold anisotropy of the surface tension  $\gamma(\bar{\alpha}) = \bar{\gamma} a_s(\bar{\alpha})$  is con-

sidered with

$$a_s(\bar{\alpha}) = 1 + \varepsilon_4 \cos(4\bar{\alpha}) \quad (16)$$

where  $\bar{\gamma}$  is the average surface tension in a (100) plane,  $\varepsilon_4$  is the strength of the surface tension anisotropy, and  $\bar{\alpha}$  is the angle between the normal to the interface and a fixed crystalline axis. For a crystal misorientation  $\alpha_0$  with respect to the coordinate axes, the anisotropy as a function of the angle  $\alpha$  between the interface normal and the axis  $x$  is

$$a_s(\alpha) = 1 + \varepsilon_4 \cos(4(\alpha - \alpha_0)) \quad (17)$$

Kinetic undercooling is also ignored, such that  $\tau_0$  can be computed as

$$\tau_0 = a_2 \lambda \frac{W^2}{D} \quad (18)$$

Thus,  $W$  is the only model parameter that should be appropriately chosen for the purpose of quantitative prediction.

Importantly, the current PF model assumes that the solid-liquid interface is at local equilibrium. As a result, it is rigorously valid in a regime for which solute trapping effect can be neglected, and hence is limited to a moderate velocity range toward the lower velocity range relevant to SLM (see Section 2.5.1).

#### 2.4.2. Polycrystalline solidification

We aim at simulating the epitaxial growth and grain growth competition of columnar grains with different crystal orientations in the melt pool, relevant to the process conditions studied here (see Section 3.2). A simple method for modeling bi-crystal grain growth competition [19] is directly extended to polycrystals. An integer field is used to store the index of grains, which has a value of  $-1$  in the liquid and a positive or zero integer value in each grain. Each index maps to a given orientation. Here, for the sake of simplicity, we consider 90 grain orientations, such that the solid grain index is taken within the range  $[0, 89]$ , which can be used directly as the value of the grain orientation in degrees. In the liquid, when  $1 - \phi^2$  exceeds a certain threshold, here fixed to 0.01, the grain index is updated to the index value most frequently present in the immediate grid point neighborhood. This method creates a thin halo of orientation field in the liquid around a grain, thus ensuring the appropriate equation is solved in the vicinity of the interface. However, when a grain index is attributed to a grid point, the crystal index field no longer evolves, and the solid-solid grain boundary will remain “frozen”. As such, this method does not take into account solid state grain boundary evolution. Yet, it remains adequate to study grain growth competition for well developed dendrites, since triple points and grain boundaries are relatively deep, and the region of interest remains close to the primary

tips. The approach has the key advantage of reducing directly to a reference, thoroughly validated, quantitative PF model at the solid-liquid interface, while being computationally efficient compared to a model using multiple order parameters (e.g. [68]).

#### 2.4.3. Numerical implementation

Equations (12) and (13) are solved in 2D on a finite-difference grid of square elements of grid spacing  $\Delta x$  using an Euler explicit time scheme with a constant time step  $\Delta t$ . The time step size is taken as 0.3 times the maximum time step based on the stability of Laplacian operators in (12) and (13). The standard second order five-point stencil is used for discretization of Laplacian operators. Other terms in (12) and (13) are discretized by central difference schemes (see appendix A and B of [19] for further details). In order to reduce the computational cost in the bulk phases away from the interface, the anisotropy terms and anti-trapping current are computed only where  $|1 - \phi^2| \geq 10^{-6}$ , i.e. in the vicinity of the solid-liquid interface. Otherwise, these terms are set to zero.

Homogeneous Neumann (no-flux) boundary conditions are applied on all domain boundaries for both PDEs. The phase-field  $\psi$  is initialized as the signed distance function to the liquidus isotherm with positive values in the solid phase. The dimensionless supersaturation field is initialized based on the equilibrium concentration over entire domain, i.e.  $U = -1$ . The grain index field is initialized to  $-1$  in the liquid region ( $\psi < 0$ ) and it is initialized to a Voronoi-based distribution of grain indices in the solid. To do so, we randomly generate  $N$  Voronoi cell centers in the entire domain using fast Poisson disk sampling [69] with a random grain index within  $[0 - 89]$ . Grain indices are then allocated to each finite difference grid point using a classical Voronoi tessellation algorithm.

The simulation domain is sized slightly larger than  $l_S \times d_S$ , in order to accommodate the entire tail of the melt pool. In order to calculate a grain map for a solidified length longer than the melt pool length, we use a standard moving frame algorithm, in which new grid points at the alloy nominal concentration are added on the right-hand side of the domain, while values of the fields at grid points leaving the simulation domain on the left-hand side are stored to be later used for reconstructing the grain map for the entire solidified length (see Figure 8).

We use  $\Delta x = 0.8W$ , and  $\Delta x$  is determined based on a convergence study monitoring the steady-state tip undercooling as a function of the grid size in unidirectional solidification considering the most computationally constraining conditions, namely the (lowest) temperature gradient and the growth velocity at the tail end of the melt pool. Under conditions relevant to additive manufacturing, such convergence study can be quite limiting, since both the dendrite tip radius

and the diffusion length are small (see section 2.5.3), but it remains critical if the objective is to quantitatively predict dendrite/cells growth kinetics and resulting grain structures. Because of this grid size limitation for quantitative predictions, PF simulations at the scale of the melt pool, even in 2D, are extremely computationally demanding. Therefore, advanced acceleration schemes are required, which we briefly mention below.

We implemented the model for parallel computing on multi-graphic processing units (Multi-GPU) using the computer unified device architecture (CUDA) programming language. Even though simulations are massively parallelized, we also aim at providing a solution that can be implemented on medium-size computing hardware accessible in-house to most research laboratories or companies. For this reason, we limit the current study to simulations performed on a single cluster node with eight Nvidia GPUs (RTX 2080Ti). A simple layer-wise domain decomposition is used, in which the computational domain is divided into 8 almost equal layers along the  $y$ -direction with a similar (total) number of grid points along  $x$ -direction. We consider one extra halo layer of points at the top and bottom rows of each domain to simplify the imposition of boundary conditions and inter-GPUs data exchange. The time loop is composed of two main kernel calls, one for the calculation of the  $\psi$ -field at the next time step and one for the calculation of the  $U$ -field at the next time step. The time stepping is then achieved by swapping pointer addresses between arrays containing values of  $\psi$  and  $U$  at the current time step and arrays containing values at the next time step. After the execution of each kernel, the halo grid data is updated by using direct GPU-GPU communication (memory copy from one GPU to its neighbor GPUs). In this way, we avoid using expensive GPU-to-CPU and CPU-to-GPU data transfer.

## 2.5. Application to Selective Laser Melting of Inconel 718 alloy

### 2.5.1. Processing conditions

We illustrate the methods described above and their coupling with the simulation of Selective Laser Melting of IN718 alloy (Table 1). Since we selected a PF model that does not account for solute trapping, it would not be appropriate to consider a laser scan velocity comparable or above the onset velocity for solute trapping. With a typical onset of solute trapping for solidification velocities on the order of  $\approx 1$  m/s, we use a scan velocity  $V = 0.1$  m/s, which should remain sufficiently below the onset of significant solute trapping. This assumption is further discussed in section 3.3.3. We consider a laser power  $P = 100$  W, relevant to actual SLM conditions of Inconel 718, which corresponds to a linear energy density  $P/V = 1.0$  J/mm [44].

### 2.5.2. Thermal simulations and parameters (FE)

The parameters used in macroscopic FE simulations are summarized in Table 2. Most material properties such as  $T_L$ ,  $T_S$ ,  $\rho(T)$ , and  $c_p(T)$  are calculated using CalPhaD. The thermal conductivity  $\kappa(T)$  is extracted from [49]. The laser absorption, convection, and emissivity coefficients are chosen according to [70]. The average powder diameter is selected equal to the layer thickness, and the view factor is chosen according to [62].

We ensured the numerical convergence of the simulation, with respect to the grid element size, the number of deposited layers, and the domain size, by monitoring the dimensions of the melt pool ( $l_S$ ,  $l_L$ ,  $d_S$ , and  $d_L$ ). We found that, in order to obtain a steady melt pool size and shape, we needed to consider (1) a minimum of two grid elements within the powder layer thickness  $h_p = 30$   $\mu\text{m}$ , and (2) at least five or six powder layers on top of the substrate considering successive heating and cooling stages, using a 0.166 s cooling time between layers, which was found to be sufficient for the part to cool down close to the external temperature. We also identified that a domain size of  $0.21 \times 1.2 \times 0.6$   $\text{mm}^3$  was sufficient to stabilize a steady melt pool. Hence, we simulated ten powder layers using a grid element size of 15  $\mu\text{m}$  and used the steady temperature profile within the tenth layer as thermal field for the PF simulations.

Moreover, in order to study the effect of the temperature-dependent properties, we performed additional simulations with either constant conductivity or constant density, all other parameters remaining the same. For these simulations, the conductivity or density of the dense material was assessed at the liquidus temperature as  $29 \text{ W}\cdot\text{m}^{-1}\cdot\text{K}^{-1}$  or  $7400 \text{ kg}\cdot\text{m}^{-3}$ , respectively. We also performed one additional simulation in which the thermal properties of the powder bed were set equal to that of the bulk (dense) material in order to estimate the effect of the difference in properties between powder bed and dense material.

### 2.5.3. Microstructure simulations and parameters (PF)

Table 3 shows the physical and computational parameters used in PF simulations. As explained in Section 2.1, the solute (Nb) partition coefficient and liquidus slope were calculated considering the full IN718 alloy (Table 1), and the corresponding pseudo-binary  $T'_M$  and  $T_0 \equiv T'_S$  used in the PF model were calculated to match the liquidus temperature  $T_L$  of the full alloy with that of the pseudo-binary approximation. Notably, the solidus temperature considered in the pseudo-binary PF simulation ( $T'_S = 1549$  K) remains close to the solidus of the full alloy calculated using CalPhaD and considered in the FE simulation ( $T_S = 1554$  K). Using ab initio molecular dynamics simulations, Walbrühl and collaborators have



Table 2: Material properties and process parameters for FE simulations.

	<b>Properties</b>	<b>Symbol</b>	<b>Value</b>	<b>Unit</b>
<b>Bulk (dense) material</b>	Solidus temp	$T_S$	1554	K
	Liquidus temp	$T_L$	1625	K
	Boiling temp	$T_V$	3038	K
	Heat capacity	$c_p$	Fig3b	$\text{J.kg}^{-1}.\text{K}^{-1}$
	Density	$\rho$	Fig3c	$\text{kg.m}^{-3}$
	Thermal conductivity	$\kappa$	Fig3d	$\text{W.m}^{-1}.\text{K}^{-1}$
<b>Powder bed</b>	Average diameter	$d$	30	$\mu\text{m}$
	Porosity	$\xi$	0.3	-
	View factor	$F$	0.33	-
<b>Gas (Argon)</b>	Density	$\rho_g$	1.66	$\text{kg.m}^3$
<b>Substrate (Stainless steel)</b>	Heat capacity	$c_p$	677	$\text{J.kg}^{-1}.\text{K}^{-1}$
	Density	$\rho$	7900	$\text{kg.m}^{-3}$
	Thermal conductivity	$\kappa$	24.9	$\text{W.m}^{-1}.\text{K}^{-1}$
<b>Process</b>	Laser Power	$P$	100	W
	Scan speed	$V$	0.1	$\text{m.s}^{-1}$
	Beam diameter	$w$	70	$\mu\text{m}$
	Thickness of layer	$h_p$	30	$\mu\text{m}$
<b>Boundary conditions</b>	Absorption coefficient	$A$	0.55	-
	Convection coefficient	$h_c$	15	$\text{W.m}^{-2}.\text{K}^{-1}$
	Emissivity	$\epsilon$	0.3	-
	External temperature	$T_{\text{ext}}$	273	K

Table 3: Material properties and process parameters for PF simulations.

<b>Properties</b>	<b>Symbol</b>	<b>Value</b>	<b>Unit</b>
Nominal alloy concentration	$c_\infty$	5.0	wt% Nb
Solute partition coefficient	$k$	0.37	-
Liquidus slope	$m$	9.0	$\text{K.wt}\% \text{Nb}^{-1}$
Liquid diffusion coefficient	$D_l$	$2.44 \times 10^{-9}$	$\text{m}^2.\text{s}^{-1}$
Pseudo-binary solvent melting temperature	$T'_M$	1670	K
Pseudo-binary reference temperature (Solidus)	$T_0$	1549	K
Gibbs-Thomson coefficient	$\Gamma$	$2.49 \times 10^{-7}$	K.m
Interface anisotropy	$\epsilon_4$	0.02	-
Grid element size	$\Delta x$	5	nm

estimated the diffusion coefficient of Nb in Ni (Ni-10at.%Nb) between 1903 and 2303 K, and assessed Arrhenius prefactor  $D_0 \approx 1.22 \times 10^{-7} \text{ m}^2/\text{s}$  and activation energy  $E \approx 55.3 \text{ kJ.mol}^{-1}.\text{K}^{-1}$  [71]. We use this expression to estimate the diffusion coefficient in the vicinity of 1700 K, which we use as constant in the PF simulation with  $D \approx 2.44 \times 10^{-9} \text{ m}^2/\text{s}$ . The Gibbs-Thomson coefficient of the solid-liquid interface is calculated as  $\Gamma = \gamma_0 T_M / L \approx 2.49 \times 10^{-7} \text{ K.m}$ , using the melting temperature of pure Ni,  $T_M = 1728 \text{ K}$ , and the latent heat of fusion,  $L = 2.08 \times 10^9 \text{ J.m}^{-3}$ , calculated from the ThermoCalc (TCNI8) calculation of  $h(T)$  for pure Ni, and an interface excess free energy  $\gamma_0 \approx 0.3 \text{ J.m}^{-2}$  consistent with those calculated for pure Ni with molecular dynamics (capillary fluctuation method) in several references (from 0.27 to 0.36  $\text{J.m}^{-2}$  in Refs [72–74]). We use an anisotropy strength for the interface excess free energy of  $\epsilon_4 = 0.02$ , which is of the same order as identified by these atomistic

simulations (e.g.  $\epsilon_4 \approx 0.018$  in [72]), considering that here we only use the fourfold anisotropy component according to Eq. (17).

For these parameters, a thorough convergence analysis (see sections 2.4.3 and 3.3.1) revealed that a grid spacing  $\Delta x = 5 \text{ nm}$  was necessary for well-converged simulations. As discussed later in section 3.3.2, this value is consistent with the relevant length scales under these conditions. Hence, considering a simulation domain size of  $250 \mu\text{m} \times 100 \mu\text{m}$ , a simulated time of 5 ms, and a stable time step  $\Delta t = 0.76 \text{ ns}$ , this resulted in  $50\,000 \times 20\,000$  grid points (i.e. over 2 billion degrees of freedom) and about 6.6 million iterations. While this is arguably a large simulation, it was nonetheless achievable in a reasonable time (under 10 days) with a reasonable computing hardware (one compute node equipped with eight Nvidia RTX 2080Ti GPUs).

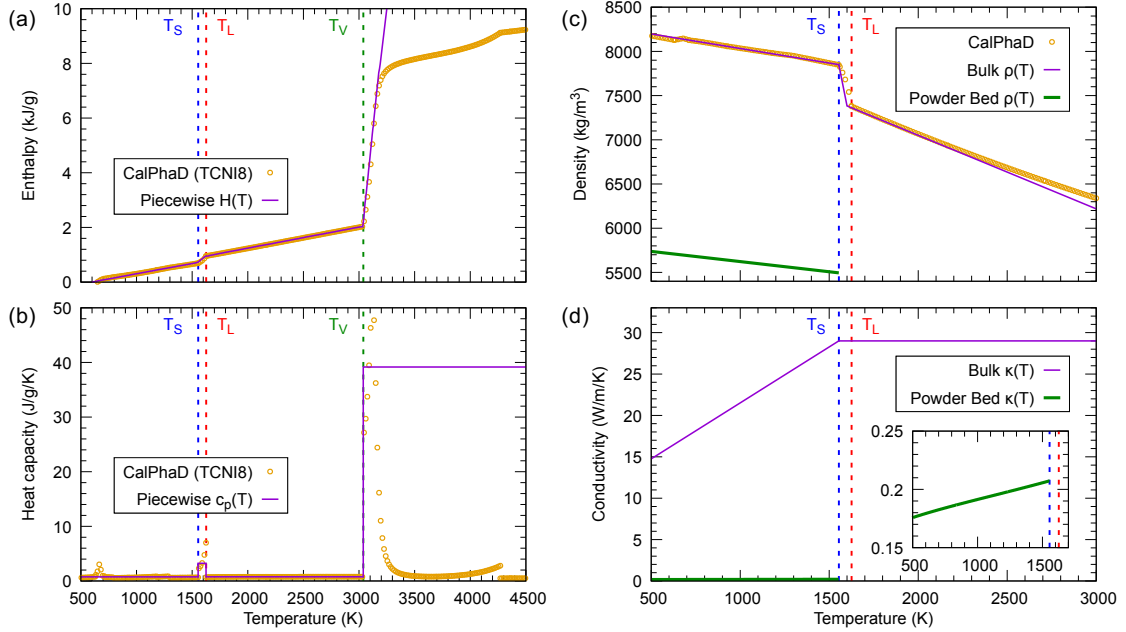


Figure 3: Temperature-dependent material properties for alloy IN718: (a) Enthalpy, (b) Heat capacity, (c) Density, (d) Conductivity [49]. CalPhaD calculated data (database TCN18) appear as symbols while piecewise linear fits used in FE simulation appear as lines (thin purple for bulk, thick green for powder bed.)

### 3. Results and Discussion

#### 3.1. Temperature-dependent thermophysical properties

In the first step of our methodology, the CalPhaD method is used to calculate the temperature-dependent properties of IN718, namely enthalpy, heat capacity, and density. Figure 3 shows the resulting CalPhaD results (orange symbols), as well as the resulting piecewise linear approximations for  $h(T)$  (i.e. piecewise constant  $c_p(T)$ ) and  $\rho(T)$  used in the FE simulations (purple solid lines). The temperature-dependent conductivity (Figure 3d) was extracted from [49]. The powder bed density and conductivity (thick green lines) are estimated using Eqs (5)-(6).

#### 3.2. Macroscopic thermal field

Figure 4 shows the temperature field during the heating stage of the tenth layer from the FE thermal simulation. The solidus and liquidus isotherms appear as blue and red lines, respectively. The resulting melt pool dimensions are  $l_L \approx 185 \mu\text{m}$ ,  $l_S \approx 249 \mu\text{m}$ ,  $d_L \approx 88 \mu\text{m}$ , and  $d_S \approx 96 \mu\text{m}$ . Note that in the PF simulations, we used approximate dimensions  $l_L = 190 \mu\text{m}$ ,  $l_S = 245 \mu\text{m}$ ,  $d_L = 90 \mu\text{m}$ , and  $d_S = 95 \mu\text{m}$ .

Figure 5a compares the tail half of the melt pool within the central longitudinal section (solid lines and symbols) with the elliptic approximation using Eqs (8)-(9) and used as input in the PF simulations (white dashed lines). Figure 5b compares the resulting temperature gradient as a function of the angle from the

top of the domain,  $\theta$ , as calculated in the FE simulations along  $T_S$  and  $T_L$  isotherms (symbols) and using the elliptic approximation (solid green line). Using the elliptic approximation, the polar component of the temperature gradient,  $(1/r)\partial T/\partial\theta$ , is the only term distinguishing the gradient measured along the solidus or along the liquidus line. Yet, its magnitude remains below  $10^4 \text{ K/m}$ , which is negligible compared to the radial component,  $\partial T/\partial r$ , which is of order  $10^6$  to  $10^7 \text{ K/m}$ . The curve in Figure 5b uses all terms along the  $T_L$  isotherm, but the plot along  $T_S$  or the plot considering only the  $\partial T/\partial r$  term are virtually undis-

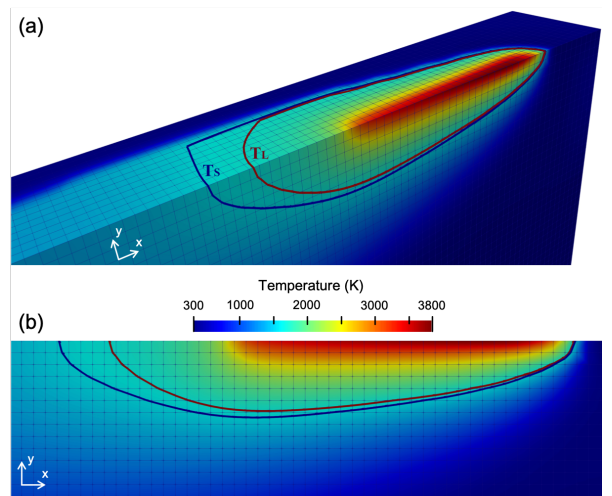


Figure 4: Temperature distribution during heating stage of tenth layer as predicted by finite element simulation.

tinguishable. Consequently, for an elliptically shaped melt pool, a reasonable estimation of the temperature gradient can be conveniently obtained directly for the polar angle as  $\partial T/\partial r = (T_L - T_S)/(r_L(\theta) - r_S(\theta))$ , using  $r_L(\theta)$  and  $r_S(\theta)$  from Eqs (8)-(9). As shown in Figure 5, in spite of a small deviation, the analytical function provides a reasonable approximation of the temperature field between  $T_L$  and  $T_S$ .

Since the growth velocity  $V_{gr}$  is at most equal to  $V = 0.1$  m/s and the temperature gradient is between  $10^6$  and  $10^7$  K/m, the ratio  $G^2/V_{gr}$  is higher than  $10^{13}$  K<sup>2</sup>s/m<sup>3</sup>, which should be sufficiently high to lead to fully epitaxial growth of columnar microstructure, consistently with the assumption made in the PF simulation. As a comparison, Knapp et al. [75] estimated the condition for a fully columnar structures for any  $G^2/V_{gr}$  above  $1.52 \times 10^{11}$  K<sup>2</sup>s/m<sup>3</sup> for Inconel 718 alloy, however considering electron beam melting.

The thermal field in Figure 4a exhibits, on the top surface, a kink in both isotherms, most prominently for the solidus, in the tail end of the melt pool. This feature is due to the presence of a straight boundary between the bulk (dense) regions directly below and behind the laser path, while the material on the side of the path is still in the powder state, hence with a significantly lower density and even more importantly a much lower conductivity (see Figure 3). Figure 6 illustrates the top surface isotherms (solid lines), as well as the computed boundary between powder bed and dense states (dashed line) for the current simula-

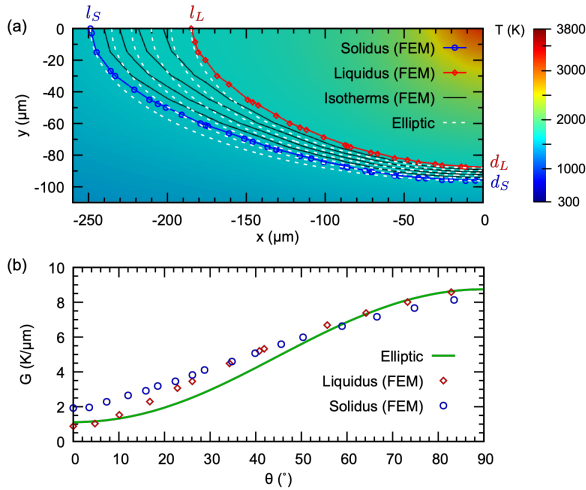


Figure 5: Melt pool shape within the longitudinal section of Figure 4b, comparing FE results and the elliptical approximation (Eq. (11)): (a) FE-predicted temperature field (color background) and isotherms for  $T = T_S = 1554$  K (solid blue line and symbols),  $T = T_L = 1625$  K (solid red line and symbols) and  $T = 1569, 1583, 1597,$  and  $1611$  K (black solid lines), compared to elliptic approximation along the same temperatures (white dashed lines); (b) temperature gradient as a function of the polar angle  $\theta$  (see Figure 2) as predicted by FE along the solidus (blue circle symbols) and liquidus (red diamond symbols) isotherms compared to the elliptic approximation (solid green line).

tion (a) as well as in a simulation in which the entire domain has the thermophysical properties of the dense material (b). Not only does the kink in both isotherm disappear, but the melt pool size is also significantly reduced in the latter case, due to the easier flow of heat along the sides made of dense more conductive material.

Finally, we also assess the effect of temperature-dependent properties on the resulting melt pool shape (liquidus and solidus isotherms) in the longitudinal section. Figure 7 shows the reference results of Figure 4 (solid lines) compared to equivalent simulations (dashed lines) considering a constant conductivity (a), constant density (b), as well as equal properties in the powder bed as in the bulk material (c). A constant

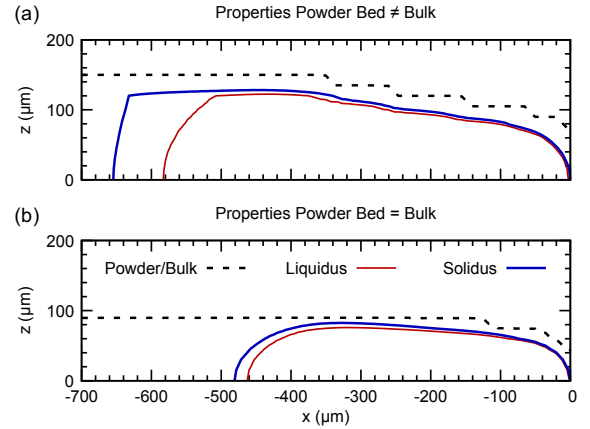


Figure 6: Top view of the liquidus and solidus isotherms (solid lines) and computed boundary between powder bed and bulk (dense) states (dashed line) when considering different thermal properties in dense and powder bed states (a), and when the powder bed has the same properties as the bulk material (b).

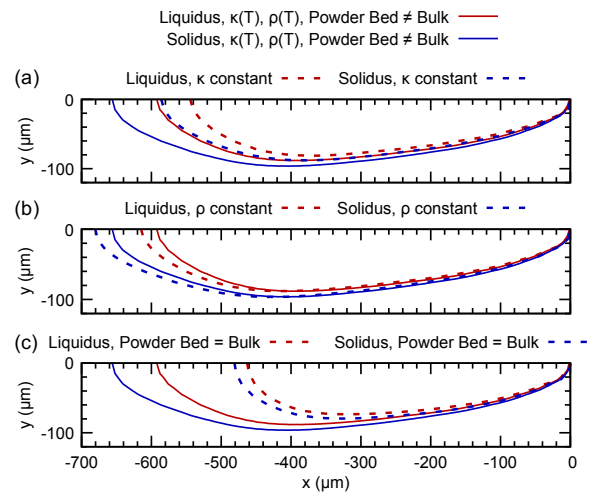


Figure 7: Liquidus (red) and solidus (blue) isotherms in the central longitudinal section for the reference simulation of Figure 4 (solid lines) compared to equivalent simulations (dashed lines) with a constant conductivity (a), constant density (b), or equal properties in the powder bed and bulk material (c).

conductivity tends to reduce the size of the melt pool, while a constant density tends to slightly increase it. However, the most important effect appears to be the consideration of different powder bed and bulk properties, as seen in Figure 7c. This was already seen in Figure 6, and further highlights the importance of accounting for the thermal properties of the powder bed in order to obtain reliable thermal simulations of powder-bed fusion processes.

### 3.3. Microstructure growth in the melt pool

#### 3.3.1. Convergence analysis

The numerical convergence analysis of our PF simulations was performed on a reduced relevant problem involving a one-dimensional thermal field, i.e. using the classical frozen temperature approximation, with a pulling velocity equal to  $V = 0.1$  m/s and a temperature gradient  $G = 10^7$  K/m. Measuring the steady state dendrite tip undercooling achieved for different grid element sizes we found that results started deviating substantially for  $\Delta x \approx 5$  nm or higher, thus identifying the grid spacing necessary to achieve quantitative simulations. Increasing the grid spacing any further promotes the interaction between neighbor dendrites and leads to the formation of pockets of highly segregated liquid between them, which resemble patterns observed in rapid solidification experiments [40, 76] but tend to disappear when the discretization is refined.

#### 3.3.2. Relevant length scales

The value of  $\Delta x \approx 5$  nm is consistent with the most important physical length scales in the melt pool solidification problem. Indeed, for  $\epsilon_4 = 0.02$ , the two-dimensional one-sided tip selection parameter is expected to be  $\sigma^* = 2Dd_0^*/(R^2V) \approx 0.15$  (see Figure 1 and Eq. (4.3) in [77]). With the alloy parameters in Table 3, an approximate estimation of the steady-state growth leads to a steady dendrite tip radius  $R \approx 39.3$  nm, with a capillary length  $d_0^* \approx 4.75$  nm at a dimensionless tip undercooling  $\Delta \approx 0.497$ , i.e. a Péclet number  $P = RV/(2D) \approx 0.806$  (whereas  $d_0$  at the solidus temperature  $T_0$  is close to 3.25 nm), and a diffusion length  $D/V = 24.4$  nm. Therefore, the grid element size  $\Delta x = 5$  nm is only eight times smaller than the steady tip radius, five times smaller than the steady diffusion length, and of the same order as the capillarity length at the tip. While only an approximate order-of-magnitude analysis (none of the actual growth in the melt ever really reaching steady state, and the laser velocity  $V$  being only relevant to the tail region of the melt pool), this still provides a sensible picture of why the grid element size cannot be taken any coarser without compromising accuracy.

#### 3.3.3. Solute trapping

Finally, we discuss the assumption of solid-liquid interface equilibrium with respect to solute trapping, and

whether a laser velocity  $V = 0.1$  m/s is sufficiently low for this assumption to remain valid. According to the continuous growth model (CGM) [78, 79], solute partitioning at the interface changes with the interface velocity  $V_i$  like  $k(V_i) = [k_e + V_i/V_D]/[1 + V_i/V_D]$ , with  $k_e$  the equilibrium partition coefficient and  $V_D$  the solute diffusion velocity through the interface. Using the parameters of the pseudo-binary alloy (Table 3) and an order of magnitude for the physical interface width  $l_A \approx 1$  nm, one can approximate the diffusion velocity as  $V_D \approx 1.44$  m/s (see Eq. (63) in [80]). Therefore, the considered laser velocity  $V = 0.1$  m/s, which is the highest growth velocity experienced in the melt pool at its tail end, seems to be sufficiently lower than  $V_D$  for solute trapping to remain negligible. However, even though we consider  $V \ll V_D$ , the resulting change of partition coefficient from the CGM is just above 10%, which remains small but could become important at larger  $V$ .

The diffuse interface width used here is  $W = 6.25$  nm, which is sensibly higher than the actual width of the solid-liquid interface. Should the required value of  $W$  be further reduced for convergence, e.g. for higher  $V$ , it is worth noting that using physically realistic diffuse interface width can lead to prediction of solute trapping effect in good agreement with the CGM [80].

#### 3.3.4. Full melt pool simulations

The results of the 2D PF simulation of solidification at the full melt pool scale appear in Figure 8, showing the time-evolution (top to bottom) of the grain structure (left) and solute (Nb) concentration field (right). The grain map illustrates the growth competition at the melt pool scale, while the solute map gives a more detailed insight into the dendritic structures within the grains. While this sole two-dimensional simulation is not sufficient to draw statistically-relevant conclusions on grain growth competition in AM-relevant conditions, trends appear that highlight interesting similarities and differences with traditional, Bridgman-like, directional solidification (DS).

Similarly to DS, dendritic elimination (impingement) and sidebranching events are responsible for the orientation selection of converging and diverging grain boundaries, respectively [19, 20] (see, e.g., top right zoomed-in regions in Figure 8, each highlighting the grain growth competition of three grains). However, in contrast with DS, the amplitude and direction of the temperature gradient, as well as the local cooling rate are constantly changing in the vicinity of each nascent grain boundary (GB). This makes it nontrivial to identify with absolute certainty the “favorably” or “unfavorably” oriented grains forming the GB, as these roles may switch during the process.

Two interesting observations can be readily made from these results. First, most grains selected by the

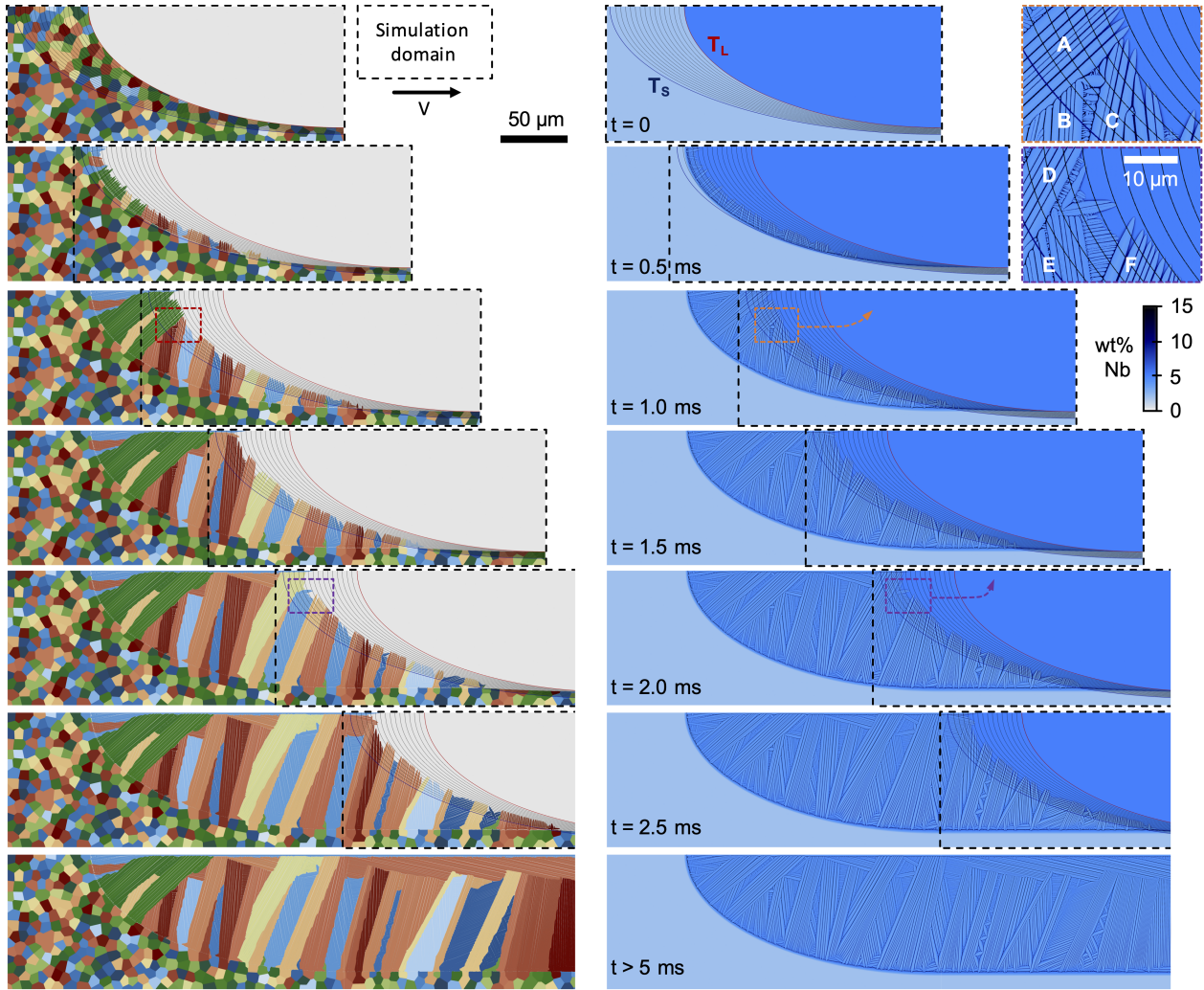


Figure 8: Phase-field simulation results showing grain structure formation (left) and solute (Nb) concentration field (right). Iso-temperature lines show  $T = T_L = 1625$  K (red),  $T = 1550$  K  $\approx T_S$  (blue), and intermediate temperature with steps of 5 K (black). The simulation domain, moving at a velocity  $V$ , is delimited with dashed black lines. Zoomed-in regions at the top right are marked with dashed rectangle in the resulting full-scale maps at  $t = 1.0$  ms and  $t = 2.0$  ms.

growth competition are slightly tilted forward with respect to the vertical direction. For most grains, this corresponds to a principal dendritic growth direction, i.e. a main crystalline orientation. However, some larger grains manage to prevail through successive sidebranching in spite of a substantial misorientation of their crystalline dendritic axes with this “mesoscopic” direction of maximum elongation of the grain (see bottom right panel in Figure 8). The prevalence of tilted columnar grains, regardless of their inner crystalline orientation, highlights the importance of the simulation at the full melt pool scale, as these would not naturally emerge from grain growth competition in a reduced subset of the melt pool.

Second, a noticeable range of different primary dendritic spacing (PDAS) range emerges (see, e.g., final, bottom-right, dendritic structure in Figure 8). This PDAS heterogeneity occurs not only among different grains but also within a same grain. Such examples

appear in the zoomed-in areas (top right) of Figure 8, most notably within grain A and grain E. Grain A exhibits a heterogeneity among spacings that emerged directly from the initial almost-planar (slightly curved) interface destabilization. Such heterogeneity may be attributed to the quasi-steady, yet not quite steady, growth conditions, combined with the fact that spacing homogenization within a grain can take substantially longer in time than it takes to reach a steady or quasi-steady growth velocity and undercooling [81]. On the other hand, the locally smaller microstructural length scale in grain E is due to the fact that the lower spacing region emerges from sidebranching, thus forming a region with locally secondary dendrite arm spacings (SDAS) along the diverging GB.

Finally, we illustrate in Figure 9 a potential use of these results in terms of digital microstructure characterization. There, we show the grain structure (color background) overlaid with the Nb concentration map

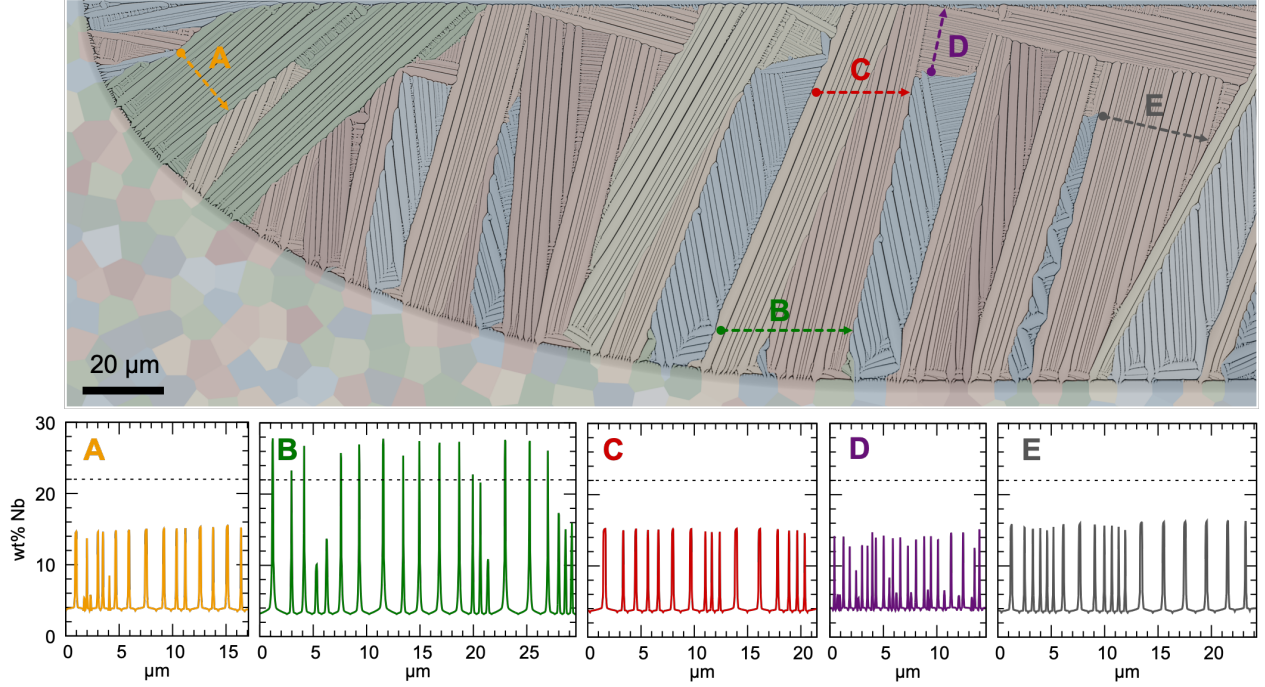


Figure 9: Solute (Nb) segregation profiles along different line scans (A–E) in the solidified region as predicted by phase-field simulations. The dashed line in the bottom plots marks the solute concentration of the eutectic point ( $L \rightarrow \text{Ni}_{\text{fcc}} + \text{Ni}_3\text{Nb}$ ) in the Ni-Nb phase diagram.

(gray level), as well as line scans of the Nb concentration in different regions of the melt pool (bottom plots). Such signals deserve two important remarks. First, periodicity of the signals gives the average primary spacing within the grain, which could be conveniently extracted in a systematic manner using adapted spectral filtering techniques. Second, the extent of interdendritic Nb segregation allows identifying the region in which the secondary phases are most prone to form. Since this composition field is reconstructed from still partially liquid regions (due to the moving frame algorithm), it is appropriate to compare these segregation peaks to the eutectic triple point ( $L \rightarrow \text{Ni}_{\text{fcc}} + \text{Ni}_3\text{Nb}$ ) at  $T \approx 1295^\circ\text{C}$  and  $c \approx 21 \text{ wt}\% \text{Nb}$  in the Ni-Nb phase diagram (according to ThermoCalc TCNI8 calculations), marked with a dashed line in the bottom plots of Figure 9. Therefore, this analysis suggests that regions at the bottom of the melt pool, such as region B, are most prone to the formation of intermetallic  $\text{Ni}_3\text{Nb}$  phase.

#### 4. Summary and Perspectives

In this article, we presented a multiscale modeling framework for the simulation of powder-bed fusion of metallic alloys. The framework combines and couples the following methods:

- CalPhaD calculation of temperature-dependent properties and phase diagram, thus allowing the investigation of alloy chemistry;

- Three-dimensional finite element thermal simulation of laser melting, considering distinct properties in distinct regions and CalPhaD-based temperature-dependent properties;
- Two-dimensional phase-field simulations of microstructure development by polycrystalline solidification in the melt pool.

We applied the methodology to simulate selective laser melting of Inconel 718 superalloy. We discussed the effect of temperature-dependent parameters and the importance applying distinct properties in the powder bed and dense regions for the prediction of the melt pool size and shape. Finally, we simulated the dynamical selection of grain structure through polycrystalline growth competition using 2D quantitative simulations at the scale of the entire melt pool, highlighting some key similarities but also differences with equivalent simulations typically performed on a reduced subset of the melt pool.

This study arguably constitutes an important step forward in the context of Integrated Computational materials Engineering (ICME) for powder-bed fusion processes. However, it also contains a number of limitations, most of which relate to ongoing work and future directions.

Regarding macroscopic simulations, the next step is a coupling with thermomechanics, including fluid dynamics, and plasticity. Simulation of fluid flow would allow predicting defect formation [10–14], but it would also permit extending the approach to powder-bed

melting in keyhole mode. If a similar level of accuracy is sought in the modeling of dendritic growth, a complete two-way coupling between solidification and fluid flow in the liquid would likely require a multiscale approach (e.g. concurrent grids or methods), a computationally efficient and scalable technique for the modeling of the flow (e.g. Lattice Boltzmann Method [82–84]), and/or advanced algorithms for code acceleration via parallelization [82, 85] and/or adaptive meshing [86–88]. Alternatively, one may also conceive a one-way coupling strategy by imposing temperature and solute fields calculated via macroscopic simulations at a distance — larger than the diffusive boundary layer yet smaller than the typical hydrodynamic length — ahead of the solidification front in microscale simulations. Ongoing extension to thermomechanics simulations in the solid state will also allow the prediction of important features related to the print quality, such as residual stresses and part distortion [13]. The level of details required to accurately predict the melt pool shape may prevent the simulation of entire components, unless leveraging advanced numerical strategies (e.g. adaptive meshing [87, 89]). However, we trust that the current physics-based approach should be scalable for the simulation of “mesoscopic” representative volume elements.

In terms of the microstructure PF simulations, main limitations relate to the pseudo-binary alloy approximation, the lack of solute trapping, and the absence of solid-state microstructure evolution. The extension to multicomponent alloys or solute trapping will require the use of dedicated models (e.g. [50–52, 54, 55]). Notably, approximate yet pragmatic extensions of the current model were recently proposed that allow some amount of solute trapping matching CGM theory at growth velocity close to  $V_D$  [56, 57]. Solid-state microstructure evolution during heat treatments, either intrinsic (e.g. in the heat affected zone) or extrinsic (e.g. via ageing), could be included asynchronously using dedicated phase-field models (e.g. [90–94]). Another important aspect to include is nucleation, since its rate determines the extent of columnar/equiaxed grain structures. Its introduction is rather straightforward using phenomenological approaches (e.g. randomly seeding nuclei) [95]. However, this would also introduce additional parameters (e.g. nuclei density and activation undercooling) which would need to be carefully calibrated to yield reliable predictions.

Ultimately, the resulting microstructure analysis proposed here remains semi-quantitative, mostly due to the two dimensional simulations, the pseudo-binary alloy approximation, and the fact that a statistical (high-throughput) exploration would be required to extract statistically meaningful trends and conclusions. However, we trust that this type of methodology offers a promising path forward for ICME in the context of alloy design and process optimization in fusion-based

AM of metals. The level of microstructural details, the limited number of calibration parameters, and the fact that such simulation is achievable using reasonable computing resources shall open the way to high-throughput statistical analyses, which will contribute to tackle the pervasive issues of uncertainty and reproducibility in metal AM.

## Acknowledgements

This investigation was supported by the Spanish Ministry of Science under the *Retos-Colaboración* project ENVIDIA (Ref. RTC-2017-6150-4). D.T. also gratefully acknowledges support from the Spanish Ministry of Science through a Ramón y Cajal Fellowship (Ref. RYC2019-028233-I).

## References

- [1] T. DebRoy, H. Wei, J. Zuback, T. Mukherjee, J. Elmer, J. Milewski, A. M. Beese, A. Wilson-Heid, A. De, W. Zhang, Additive manufacturing of metallic components—process, structure and properties, *Progress in Materials Science* 92 (2018) 112–224.
- [2] C. Kuehmann, G. Olson, Computational materials design and engineering, *Materials Science and Technology* 25 (4) (2009) 472–478.
- [3] J. Allison, Integrated computational materials engineering: A perspective on progress and future steps, *Jom* 63 (4) (2011) 15.
- [4] J. H. Panchal, S. R. Kalidindi, D. L. McDowell, Key computational modeling issues in integrated computational materials engineering, *Computer-Aided Design* 45 (1) (2013) 4–25.
- [5] W. Xiong, G. B. Olson, Integrated computational materials design for high-performance alloys, *MRS Bulletin* 40 (12) (2015) 1035–1044.
- [6] M. M. Francois, A. Sun, W. E. King, N. J. Henson, D. Tourret, C. A. Bronkhorst, N. N. Carlson, C. K. Newman, T. Haut, J. Bakosi, et al., Modeling of additive manufacturing processes for metals: Challenges and opportunities, *Current Opinion in Solid State and Materials Science* 21 (4) (2017) 198–206.
- [7] C. Körner, M. Markl, J. A. Koepf, Modeling and simulation of microstructure evolution for additive manufacturing of metals: a critical review, *Metallurgical and Materials Transactions A* 51 (10) (2020) 4970–4983.
- [8] T. DebRoy, T. Mukherjee, H. Wei, J. Elmer, J. Milewski, Metallurgy, mechanistic models and machine learning in metal printing, *Nature Reviews Materials* 6 (1) (2021) 48–68.
- [9] A. Otto, M. Schmidt, Towards a universal numerical simulation model for laser material processing, *Physics Procedia* 5 (2010) 35–46.
- [10] S. A. Khairallah, A. T. Anderson, A. Rubenchik, W. E. King, Laser powder-bed fusion additive manufacturing: Physics of complex melt flow and formation mechanisms of pores, spatter, and denudation zones, *Acta Materialia* 108 (2016) 36–45.
- [11] C. Panwisawas, B. Perumal, R. M. Ward, N. Turner, R. P. Turner, J. W. Brooks, H. C. Basoalto, Keyhole formation and thermal fluid flow-induced porosity during laser fusion welding in titanium alloys: Experimental and modelling, *Acta Materialia* 126 (2017) 251–263.
- [12] W. Yan, W. Ge, Y. Qian, S. Lin, B. Zhou, W. K. Liu, F. Lin, G. J. Wagner, Multi-physics modeling of single/multi-track defect mechanisms in electron beam selective melting, *Acta Materialia* 134 (2017) 324–333.

- [13] Y. Zhang, Q. Chen, G. Guillemot, C.-A. Gandin, M. Bellet, Numerical modelling of fluid and solid thermomechanics in additive manufacturing by powder-bed fusion: Continuum and level set formulation applied to track-and part-scale simulations, *Comptes Rendus Mécanique* 346 (11) (2018) 1055–1071.
- [14] C. Tang, K. Le, C. Wong, Physics of humping formation in laser powder bed fusion, *International Journal of Heat and Mass Transfer* 149 (2020) 119172.
- [15] L.-X. Lu, N. Sridhar, Y.-W. Zhang, Phase field simulation of powder bed-based additive manufacturing, *Acta Materialia* 144 (2018) 801–809.
- [16] Y. Yang, O. Ragnvaldsen, Y. Bai, M. Yi, B.-X. Xu, 3D non-isothermal phase-field simulation of microstructure evolution during selective laser sintering, *npj Computational Materials* 5 (1) (2019) 1–12.
- [17] M. Yang, L. Wang, W. Yan, Phase-field modeling of grain evolutions in additive manufacturing from nucleation, growth, to coarsening, *Npj Computational Materials* 7 (1) (2021) 1–12.
- [18] A. F. Chadwick, P. W. Voorhees, The development of grain structure during additive manufacturing, *Acta Materialia* 211 (2021) 116862.
- [19] D. Tourret, A. Karma, Growth competition of columnar dendritic grains: A phase-field study, *Acta Materialia* 82 (2015) 64–83.
- [20] D. Tourret, Y. Song, A. J. Clarke, A. Karma, Grain growth competition during thin-sample directional solidification of dendritic microstructures: A phase-field study, *Acta Materialia* 122 (2017) 220–235.
- [21] T. M. Rodgers, J. D. Madison, V. Tikare, Simulation of metal additive manufacturing microstructures using kinetic Monte Carlo, *Computational Materials Science* 135 (2017) 78–89.
- [22] H. Wei, J. Elmer, T. DebRoy, Crystal growth during key-hole mode laser welding, *Acta Materialia* 133 (2017) 10–20.
- [23] M. Rappaz, C.-A. Gandin, Probabilistic modelling of microstructure formation in solidification processes, *Acta metallurgica et materialia* 41 (2) (1993) 345–360.
- [24] C.-A. Gandin, M. Rappaz, A coupled finite element-cellular automaton model for the prediction of dendritic grain structures in solidification processes, *Acta metallurgica et materialia* 42 (7) (1994) 2233–2246.
- [25] S. Chen, G. Guillemot, C.-A. Gandin, Three-dimensional cellular automaton-finite element modeling of solidification grain structures for arc-welding processes, *Acta materialia* 115 (2016) 448–467.
- [26] A. Rai, M. Markl, C. Körner, A coupled cellular automaton–lattice Boltzmann model for grain structure simulation during additive manufacturing, *Computational Materials Science* 124 (2016) 37–48.
- [27] J. Koepf, D. Soldner, M. Ramsperger, J. Mergheim, M. Markl, C. Körner, Numerical microstructure prediction by a coupled finite element cellular automaton model for selective electron beam melting, *Computational Materials Science* 162 (2019) 148–155.
- [28] Y. Lian, Z. Gan, C. Yu, D. Kats, W. K. Liu, G. J. Wagner, A cellular automaton finite volume method for microstructure evolution during additive manufacturing, *Materials & Design* 169 (2019) 107672.
- [29] M. S. Mohebbi, V. Ploshikhin, Implementation of nucleation in cellular automaton simulation of microstructural evolution during additive manufacturing of Al alloys, *Additive Manufacturing* 36 (2020) 101726.
- [30] A. Pineau, G. Guillemot, D. Tourret, A. Karma, C.-A. Gandin, Growth competition between columnar dendritic grains – Cellular automaton versus phase field modeling, *Acta Materialia* 155 (2018) 286–301.
- [31] E. Dorari, K. Ji, G. Guillemot, C.-A. Gandin, A. Karma, Growth competition between columnar dendritic grains – The role of microstructural length scales, *Acta Materialia* (2021) 117395.
- [32] W. J. Boettinger, J. A. Warren, C. Beckermann, A. Karma, Phase-field simulation of solidification, *Annual review of materials research* 32 (1) (2002) 163–194.
- [33] L.-Q. Chen, Phase-field models for microstructure evolution, *Annual review of materials research* 32 (1) (2002) 113–140.
- [34] N. Moelans, B. Blanpain, P. Wollants, An introduction to phase-field modeling of microstructure evolution, *Calphad* 32 (2) (2008) 268–294.
- [35] I. Steinbach, Phase-field models in materials science, Modelling and simulation in materials science and engineering 17 (7) (2009) 073001.
- [36] I. Steinbach, Phase-field model for microstructure evolution at the mesoscopic scale, *Annual Review of Materials Research* 43 (2013) 89–107.
- [37] D. Tourret, H. Liu, J. LLorca, Phase-field modeling of microstructure evolution: Recent applications, perspectives and challenges, *Progress in Materials Science* 123 (2022) 100810.
- [38] A. Karma, W. Rappel, Quantitative phase-field modeling of dendritic growth in two and three dimensions, *Physical Review E* 57 (4) (1998) 4323.
- [39] B. Echebarria, R. Folch, A. Karma, M. Plapp, Quantitative phase-field model of alloy solidification, *Physical Review E* 70 (6) (2004) 061604.
- [40] T. Keller, G. Lindwall, S. Ghosh, L. Ma, B. M. Lane, F. Zhang, U. R. Kattner, E. A. Lass, J. C. Heigel, Y. Idell, et al., Application of finite element, phase-field, and CALPHAD-based methods to additive manufacturing of ni-based superalloys, *Acta materialia* 139 (2017) 244–253.
- [41] G. Boussinot, M. Apel, J. Zielinski, U. Hecht, J. Schleifenbaum, Strongly out-of-equilibrium columnar solidification during laser powder-bed fusion in additive manufacturing, *Physical Review Applied* 11 (1) (2019) 014025.
- [42] J. Kundin, A. Ramazani, U. Prah, C. Haase, Microstructure evolution of binary and multicomponent manganese steels during selective laser melting: phase-field modeling and experimental validation, *Metallurgical and Materials Transactions A* 50 (4) (2019) 2022–2040.
- [43] T. Pinomaa, M. Lindroos, M. Walbrühl, N. Provatas, A. Laukkanen, The significance of spatial length scales and solute segregation in strengthening rapid solidification microstructures of 316L stainless steel, *Acta Materialia* 184 (2020) 1–16.
- [44] K. Karayagiz, L. Johnson, R. Seede, V. Attari, B. Zhang, X. Huang, S. Ghosh, T. Duong, I. Karaman, A. Elwany, et al., Finite interface dissipation phase field modeling of Ni–Nb under additive manufacturing conditions, *Acta Materialia* 185 (2020) 320–339.
- [45] V. Fallah, M. Amoozezaei, N. Provatas, S. Corbin, A. Khajepour, Phase-field simulation of solidification morphology in laser powder deposition of Ti–Nb alloys, *Acta Materialia* 60 (4) (2012) 1633–1646.
- [46] J. Berry, A. Perron, J.-L. Fattebert, J. D. Roehling, B. Vrancken, T. T. Roehling, D. L. Rosas, J. A. Turner, S. A. Khairallah, J. T. McKeown, et al., Toward multiscale simulations of tailored microstructure formation in metal additive manufacturing, *Materials Today* 51 (2021) 65–86.
- [47] F. Yu, Y. Wei, X. Liu, The evolution of polycrystalline solidification in the entire weld: A phase-field investigation, *International Journal of Heat and Mass Transfer* 142 (2019) 118450.
- [48] W. Kurz, D. J. Fisher, *Fundamentals of solidification*, 1984.
- [49] K. C. Mills, Recommended values of thermophysical properties for selected commercial alloys, Woodhead Publishing, 2002.
- [50] J. Eiken, B. Böttger, I. Steinbach, Multiphase-field approach for multicomponent alloys with extrapolation scheme for numerical application, *Physical review E* 73 (6) (2006) 066122.
- [51] B. Nestler, A. Choudhury, Phase-field modeling of multi-component systems, *Current opinion in solid state and Ma-*



- terials Science 15 (3) (2011) 93–105.
- [52] M. Ohno, Quantitative phase-field modeling of nonisothermal solidification in dilute multicomponent alloys with arbitrary diffusivities, *Physical Review E* 86 (5) (2012) 051603.
- [53] I. Steinbach, L. Zhang, M. Plapp, Phase-field model with finite interface dissipation, *Acta Materialia* 60 (6-7) (2012) 2689–2701.
- [54] L. Zhang, I. Steinbach, Phase-field model with finite interface dissipation: Extension to multi-component multi-phase alloys, *Acta Materialia* 60 (6-7) (2012) 2702–2710.
- [55] J. Kundin, L. Mushongera, H. Emmerich, Phase-field modeling of microstructure formation during rapid solidification in Inconel 718 superalloy, *Acta Materialia* 95 (2015) 343–356.
- [56] T. Pinomaa, N. Provatas, Quantitative phase field modeling of solute trapping and continuous growth kinetics in quasi-rapid solidification, *Acta Materialia* 168 (2019) 167–177.
- [57] S. Kavousi, M. A. Zaeem, Quantitative phase-field modeling of solute trapping in rapid solidification, *Acta Materialia* 205 (2021) 116562.
- [58] S. G. Kim, W. T. Kim, P.-R. Cha, B.-J. Lee, J. S. Lee, J. Park, C.-S. Oh, Phase-field model with relaxation of the partition coefficient, *Computational Materials Science* 188 (2021) 110184.
- [59] K. Karayagiz, A. Elwany, G. Tapia, B. Franco, L. Johnson, J. Ma, I. Karaman, R. Arróyave, Numerical and experimental analysis of heat distribution in the laser powder bed fusion of Ti-6Al-4V, *IJSE Transactions* 51 (2) (2019) 136–152.
- [60] L.-E. Loh, C.-K. Chua, W.-Y. Yeong, J. Song, M. Mapar, S.-L. Sing, Z.-H. Liu, D.-Q. Zhang, Numerical investigation and an effective modelling on the selective laser melting (SLM) process with aluminium alloy 6061, *International Journal of Heat and Mass Transfer* 80 (2015) 288–300.
- [61] A. Iveković, M. L. Montero-Sistiaga, J. Vleugels, J.-P. Kruth, K. Vanmeensel, Crack mitigation in laser powder bed fusion processed Hastelloy X using a combined numerical-experimental approach, *Journal of Alloys and Compounds* 864 (2021) 158803.
- [62] S. S. Sih, J. W. Barlow, The prediction of the emissivity and thermal conductivity of powder beds, *Particulate science and technology* 22 (4) (2004) 427–440.
- [63] G. Damköhler, Einflüsse der strömung, diffusion und des wärmeüberganges auf die leistung von reaktionsöfen.: I. Allgemeine Gesichtspunkte für die übertragung eines chemischen prozesses aus dem kleinen ins große, *Zeitschrift für Elektrochemie und angewandte physikalische Chemie* 42 (12) (1936) 846–862.
- [64] P. Zehner, E. Schlünder, Wärmeleitfähigkeit von schüttungen bei mäßigen temperaturen, *Chemie Ingenieur Technik* 42 (14) (1970) 933–941.
- [65] D. Portillo, D. del Pozo, D. Rodríguez-Galán, J. Segurado, I. Romero, MUESLI - a Material UnivErSal Library, *Advances in Engineering Software* 105 (2017) 1–8.
- [66] V. Thomée, Galerkin Finite Element Methods for Parabolic Problems, Vol. 25 of Springer Series in Computational Mathematics, Springer Science & Business Media, Berlin, Heidelberg, 1997.
- [67] K. Glasner, Nonlinear preconditioning for diffuse interfaces, *J Comput Phys* 174 (2) (2001) 695–711.
- [68] I. Steinbach, F. Pezzolla, B. Nestler, M. Seeßelberg, R. Prieler, G. Schmitz, J. Rezende, A phase field concept for multiphase systems, *Physica D: Nonlinear Phenomena* 94 (3) (1996) 135–147.
- [69] R. Bridson, Fast Poisson disk sampling in arbitrary dimensions, *SIGGRAPH sketches* 10 (1) (2007).
- [70] Y. Zhang, L. Wu, X. Guo, S. Kane, Y. Deng, Y.-G. Jung, J.-H. Lee, J. Zhang, Additive manufacturing of metallic materials: a review, *Journal of Materials Engineering and Performance* 27 (1) (2018) 1–13.
- [71] M. Walbrühl, A. Blomqvist, P. A. Korzhavyi, Atomic diffusion in liquid nickel: First-principles modeling, *The Journal of chemical physics* 148 (24) (2018) 244503.
- [72] J. J. Hoyt, M. Asta, A. Karma, Atomistic and continuum modeling of dendritic solidification, *Materials Science and Engineering: R: Reports* 41 (6) (2003) 121–163.
- [73] Q. Jiang, H. Lu, Size dependent interface energy and its applications, *Surface Science Reports* 63 (10) (2008) 427–464.
- [74] E. Asadi, M. A. Zaeem, S. Nouranian, M. I. Baskes, Two-phase solid–liquid coexistence of Ni, Cu, and Al by molecular dynamics simulations using the modified embedded-atom method, *Acta Materialia* 86 (2015) 169–181.
- [75] G. L. Knapp, N. Raghavan, A. Plotkowski, T. Debroy, Experiments and simulations on solidification microstructure for Inconel 718 in powder bed fusion electron beam additive manufacturing, *Additive Manufacturing* 25 (2019) 511–521.
- [76] W. Boettinger, L. Bendersky, R. Schaefer, F. Biancaniello, On the formation of dispersoids during rapid solidification of an Al-Fe-Ni alloy, *Metallurgical Transactions A* 19 (4) (1988) 1101–1107.
- [77] A. Barbieri, J. Langer, Predictions of dendritic growth rates in the linearized solvability theory, *Physical Review A* 39 (10) (1989) 5314.
- [78] M. J. Aziz, Model for solute redistribution during rapid solidification, *Journal of Applied Physics* 53 (2) (1982) 1158–1168.
- [79] M. J. Aziz, T. Kaplan, Continuous growth model for interface motion during alloy solidification, *Acta metallurgica* 36 (8) (1988) 2335–2347.
- [80] N. Ahmad, A. Wheeler, W. J. Boettinger, G. B. McFadden, Solute trapping and solute drag in a phase-field model of rapid solidification, *Physical Review E* 58 (3) (1998) 3436.
- [81] A. Clarke, D. Tourret, Y. Song, S. Imhoff, P. Gibbs, J. Gibbs, K. Fezzaa, A. Karma, Microstructure selection in thin-sample directional solidification of an Al-Cu alloy: In situ X-ray imaging and phase-field simulations, *Acta Materialia* 129 (2017) 203–216.
- [82] S. Sakane, T. Takaki, R. Rojas, M. Ohno, Y. Shibuta, T. Shimokawabe, T. Aoki, Multi-GPU parallel computation of dendrite growth in forced convection using the phase-field-lattice Boltzmann model, *Journal of Crystal Growth* 474 (2017) 154–159.
- [83] T. Takaki, S. Sakane, M. Ohno, Y. Shibuta, T. Aoki, Large-scale phase-field lattice Boltzmann study on the effects of natural convection on dendrite morphology formed during directional solidification of a binary alloy, *Computational Materials Science* 171 (2020) 109209.
- [84] N. Yamanaka, S. Sakane, T. Takaki, Multi-phase-field lattice Boltzmann model for polycrystalline equiaxed solidification with motion, *Computational Materials Science* 197 (2021) 110658.
- [85] T. Shimokawabe, T. Aoki, T. Takaki, T. Endo, A. Yamanaka, N. Maruyama, A. Nukada, S. Matsuoka, Petascale phase-field simulation for dendritic solidification on the TSUBAME 2.0 supercomputer, in: *Proceedings of 2011 International Conference for High Performance Computing, Networking, Storage and Analysis*, 2011, pp. 1–11.
- [86] M. Greenwood, K. Shampur, N. Ofori-Opoku, T. Pinomaa, L. Wang, S. Gurevich, N. Provatas, Quantitative 3D phase field modelling of solidification using next-generation adaptive mesh refinement, *Computational Materials Science* 142 (2018) 153–171.
- [87] Y. Zhang, G. Guillemot, M. Bernacki, M. Bellet, Macroscopic thermal finite element modeling of additive metal manufacturing by selective laser melting process, *Computer Methods in Applied Mechanics and Engineering* 331 (2018) 514–535.
- [88] S. Sakane, T. Takaki, T. Aoki, Parallel-GPU-accelerated adaptive mesh refinement for three-dimensional phase-field simulation of dendritic growth during solidification of binary alloy, *Materials Theory* 6 (1) (2022) 1–19.
- [89] J. Baiges, M. Chiumenti, C. A. Moreira, M. Cervera, R. Codina, An adaptive finite element strategy for the numerical

- simulation of additive manufacturing processes, *Additive Manufacturing* 37 (2021) 101650.
- [90] Y. Wen, J. Simmons, C. Shen, C. Woodward, Y. Wang, Phase-field modeling of bimodal particle size distributions during continuous cooling, *Acta materialia* 51 (4) (2003) 1123–1132.
- [91] J. Zhu, T. Wang, A. Ardell, S. Zhou, Z. Liu, L. Chen, Three-dimensional phase-field simulations of coarsening kinetics of  $\gamma'$  particles in binary Ni–Al alloys, *Acta materialia* 52 (9) (2004) 2837–2845.
- [92] G. Boussinot, A. Finel, Y. Le Bouar, Phase-field modeling of bimodal microstructures in nickel-based superalloys, *Acta Materialia* 57 (3) (2009) 921–931.
- [93] M. Cottura, Y. Le Bouar, A. Finel, B. Appolaire, K. Ammar, S. Forest, A phase field model incorporating strain gradient viscoplasticity: application to rafting in Ni-base superalloys, *Journal of the Mechanics and Physics of Solids* 60 (7) (2012) 1243–1256.
- [94] M. A. Ali, J. V. Görler, I. Steinbach, Role of coherency loss on rafting behavior of Ni-based superalloys, *Computational Materials Science* 171 (2020) 109279.
- [95] L. Gránásy, G. I. Tóth, J. A. Warren, F. Podmaniczky, G. Tegze, L. Rátkai, T. Pusztai, Phase-field modeling of crystal nucleation in undercooled liquids – A review, *Progress in Materials Science* 106 (2019) 100569.